Chinese Chemical Letters 34 (2023) 107597

Contents lists available at ScienceDirect

Chinese Chemical Letters

journal homepage: www.elsevier.com/locate/cclet

CoS_2/N,S co-doped mesoporous carbon with 3D micro-nano crosslinked structure as efficient bifunctional oxygen electrocatalysts for zinc-air batteries

Wei Wang[a,b,c], Liqin Li[a], Jie Ouyang[a,d], Jialin Gong[a], Jie Tian[a], Liang Chen[a], Junlin Huang[a], Binhong He[a], Zhaohui Hou[a,*]

[a] Key Laboratory of Hunan Province for Advanced Carbon-based Functional Materials, School of Chemistry and Chemical Engineering, Hunan Institute of Science and Technology, Yueyang 414006, China
[b] Guangxi Key Laboratory of Low Energy Material, Guangxi Normal University, Guilin 541004, China
[c] Hubei Key Laboratory of Pollutant Analysis & Reuse Technology, Hubei Normal University, Huangshi 435002, China
[d] Hunan Province Key Laboratory of Materials Surface & Interface Science and Technology, Material Science and Engineering School, Central South University of Forestry and Technology, Changsha 410004, China

ARTICLE INFO

Article history:
Received 27 April 2022
Revised 28 May 2022
Accepted 8 June 2022
Available online 13 June 2022

Keywords:
Micro-nano crosslinked
CoS_2
ORR
OER
Zn-air battery

ABSTRACT

This work describes a bifunctional oxygen catalyst made of cobalt disulfide encapsulated in N,S co-doped mesoporous carbon with a novel three-dimensional micro-nano crosslinking structure. The proposed composite materials exhibit promising oxygen electrocatalytic activity and stability. The composite assembled rechargeable zinc-air battery can achieve a high power density of 208.9 mW/cm^2, and can be stably cycled for more than 160 h. Additionally, the all-solid zinc-air battery assembled with the electrocatalyst also performs admirably. The micro-nano crosslinking and high porosity structure, as well as the large number of active sites generated by the synergy of N,S doping and the close interface between carbon matrix and CoS_2, contribute to the composite's exceptional electrochemical performance. This study's rational strategy lays the path for the development of other high-performance bifunctional electrocatalysts.

Zinc-air battery (ZAB) is a candidate for advanced energy technology due to high theoretical energy density (1086 Wh/kg) and good safety [1]. However, the high overpotential and slow kinetic efficiency of the oxygen reduction and oxygen evolution reactions (ORR and OER) limit its commercial application significantly [2,3]. At present, noble metal electrocatalysts exhibit the highest oxygen electrocatalytic efficiency, but single component noble metal catalysts lack bifunctional oxygen catalysis ability, which severely restricts its development [4].

Cobalt-based materials, particularly sulfides, have garnered considerable attention in recent years due to their comparatively high oxygen electrocatalytic activity, low cost, and excellent stability [5]. Its sulfides exhibit a broad variety of crystal morphologies and stoichiometric compositions, including Co_3S_4 [6], CoS_2 [7], CoS [8], Co_9S_8 [9] and others [10]. Several investigations have demonstrated that the oxygen electrocatalytic performance of cobalt sulphide is determined by the crystal and micro-nano structure [11–14]. However, the low conductivity and dispersibility, limiting its development and application. Taking advantage of the electrical conductivity, large surface area and nano-confined effect of carbonaceous materials, it is an effective strategy to design composites of transition metal materials and carbonaceous materials in which the carbonaceous material acts as matrix, not only forming a conductive framework, but also ensuring the stability [15–17]. For instance, based on the advantages of ordered mesoporous carbon materials, such as a high specific surface area, regular mesoporous pores, and an abundance of defect sites, it can be utilized as a matrixt for TMS catalysts to significantly improve their performance [18,19]. On the one hand, mesoporous carbon materials can improve the electrical conductivity of composites through the internal conductive network formed [20]. On the other hand, the high specific surface area, extensive defects, and edge positions created by the micro-nano crosslinking structure of mesoporous carbon materials contribute to the stability of metal-based materials, resulting in a uniform distribution of electrocatalytic active sites [21]. Simultaneously, the pore structure can be used to shorten the diffusion

* Corresponding author.
E-mail address: zhaohuihou@126.com (Z. Hou).

https://doi.org/10.1016/j.cclet.2022.06.020
1001-8417/

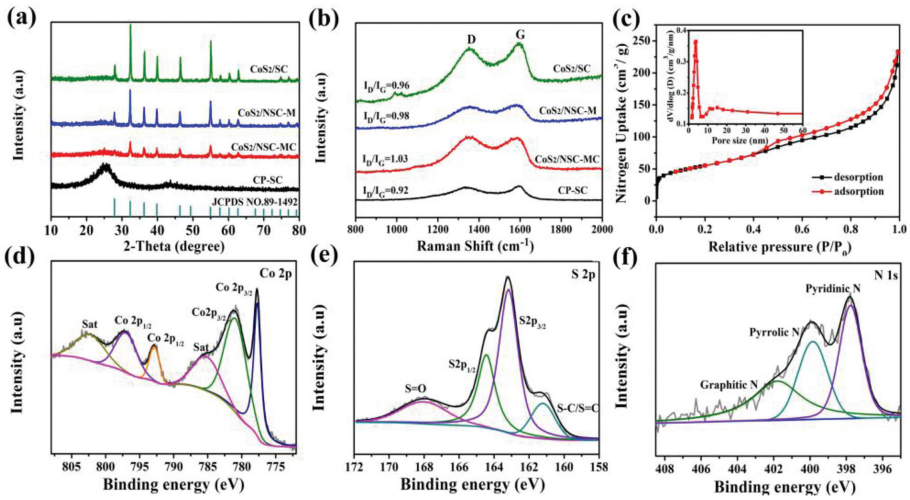

Fig. 1. (a) XRD patterns and (b) Raman spectra of CP-SC, CoS_2/SC, CoS_2/NSC-M and CoS_2/NSC-MC. (c) N_2 adsorption-desorption isotherms, the insert is BJH pore-size distribution of CoS_2/NSC-MC. (d-f) High-resolution spectra of Co 2p, S 2p and N 1s for CoS_2/NSC-MC, respectively.

mean-free path of reactants, hence enhancing mass transfer efficiency [22].

Nitrogen and sulfur heteroatom doping can enhance the active sites and wettability on carbon surfaces, in attempt to optimise the oxygen electrochemical performance [23,24]. Multi-heteroatom codoping can further enhance the ORR activity of single heteroatom-doped carbon materials through synergistic effect [25–27]. Besides, the active sites containing transition metals are typically thought to have higher ORR activity than non-metallic heteroatom-doped carbon, and several researchers have confirmed that transition metal sulphides, especially cobalt sulphide, are an excellent catalyst for OER [28,29]. As a result, the developing composite materials capable of bifunctional catalysis of OER and ORR is a good choice for them using in reversible metal-air batteries, including zinc-air batteries [30–32].

In this paper, CoS_2 nanocrystals encapsulated in ordered mesoporous carbon composites were prepared by combining metal materials with pitch-derived carbon through 2-methylimidazole with an aromatic ring, with pitch serving as the carbon source and SBA-15 serving as the template. Along with uniform pores, the material exhibits optimised micro-nano crosslinking structure. The reversible zinc-air battery using this composite, in particular, has a highest power density of 208.9 mW/cm^2 and can stabilize the charge-discharge cycle for more than 160 h, which is significantly better than the commercial Pt/RuO_2/C electrocatalyst.

By studying the XRD spectrum of the composites (Fig. 1a), the CP-SC exhibits diffraction peaks corresponding to the (002) and (100) crystal planes of graphitized carbon, suggesting that the pitch has been entirely carbonised. The characteristic diffraction peaks for CoS_2/SC, CoS_2/NSC-M, and CoS_2/NSC-MC samples corresponding to the standard CoS_2 (JCPDS No. 89-1492). Due to the fact that their calcination temperatures are identical, the weak diffraction peaks of CoS_2/NSC-MC is dependent on the small particle size of the metal nanocrystals. This demonstrates that combine the coordination of 2-methylimidazole and the dispersion of β-cyclodextrin, the particle size of CoS_2 particles could be significantly regulated, therefore more active sites become exposed.

Raman spectra (Fig. 1b) of the samples exhibit two characteristic peaks at 1351 cm^{-1} and 1586 cm^{-1} which correspond to the D band of defective carbon and the G band of graphite carbon, respectively. Compare with the samples, the defect ratio of CoS_2/SC ($I_D/I_G = 0.96$) is higher than that of CP-SC ($I_D/I_G = 0.92$), indicating that the interaction between metal and carbon can cause defects in carbonaceous matrix. CoS_2/NSC-M and CoS_2/NSC-MC exhibit high I_D/I_G values of 0.98 and 1.03, respectively, due to the doping of nitrogen atoms in mesoporous carbon by 2-methylimidazole, and also due to the influence of 2-methylimidazole and cyclodextrin on the particle size and uniform distribution of CoS_2.

For study the specific surface area and pore structure of the materials, N_2 adsorption and desorption tests were carried out. The samples exhibited type IV adsorption-desorption isotherms with H3 hysteresis loop (Fig. 1c and Fig. S1a in Supporting information), confirming the presence of mesoporous structure in the materials [33]. The related pore size distribution curves (the insert in Fig. 1c and Fig. S1b in Supporting information) corroborate this conclusion. Table S1 (Supporting information) summarises the specific surface area, pore volume, and average pore size of the samples. The specific surface area of CoS_2/NSC-MC (194.9 m^2/g) is less than that of CP-SC (288.8 m^2/g), which is due to the occupation result of CoS_2 on carbonaceous matrix. Additionally, the presence of CoS_2 results in a large pore size, and CoS_2/NSC-MC has the largest pore volume, which is expected to increase the density of active sites while improving the diffusion efficiency of oxygen catalysis-related species (such as O_2, OH^-), thereby improving the oxygen electrocatalytic performance [34].

X-ray photoelectron spectroscopy (XPS) was used to investigate the surface chemical composition and chemical bond of CoS_2/NSC-MC. The characteristic peaks of CoS_2/NSC-MC in the XPS survey spectrum (Fig. S2a in Supporting information) can be assigned to the elements C, Co, S, N and O. The embedded graphic illustrates the contents of the material surface in terms of C (76.77%), Co (1.95%), S (11.51%), N (2.24%) and O (7.53%), respectively. The low Co content may be due to that many embedded CoS_2 in the carbon matrix cannot be detected by XPS. High resolution spectrum of Co 2p (Fig. 1d) can be deconvoluted into six peaks, with binding energy of 796.9 and 780.89 eV corresponding to $2p_{1/2}$ and $2p_{3/2}$ of highly oxidation state Co, respectively, and 792.8 and 777.7 eV corresponding to low oxidation state Co [35]. Additionally, the two satellite peaks at 802.2 and 785.1 eV are ascribed to the oscillatory excitation of high spin Co ions [36]. For the high resolution spectrum of S 2p (Fig. 1e), the two fitting peaks at 163.2 eV and 164.4 eV can be attributed to the lattice sulfur in CoS_2, confirming the successful synthesis of CoS_2, whereas the peak at 161.2 eV belongs to the S=C/S-C structure and the peak at 168 eV belongs to the S-O structure [37,38]. The O1s high resolution spectra (Fig. S2b in Supporting information) can be deconvoluted into two peaks corresponding to O=C-O (531.2 eV) and surface hydroxyl (532.9 eV), indicating the absence of cobalt oxide lattice oxygen [39]. The N 1s

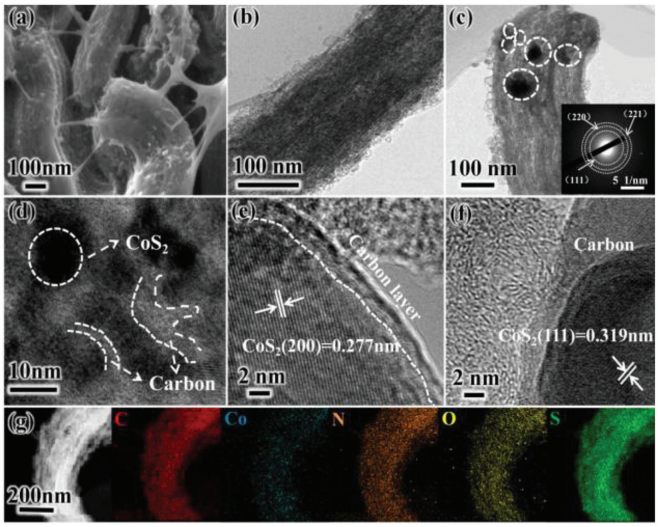

Fig. 2. (a) SEM of CoS_2/NSC-MC. TEM of CoS_2/NSC-MC: (b-d) TEM, the insert is SAED patterns, (e, f) HRTEM, (g) elemental mapping.

high resolution spectrum of CoS_2/NSC-MC is shown in Fig. 1f. The three peaks between 397.7, 399.8 and 401.7 eV correspond to pyridine N (37.68%), pyrrole N (32.86%), and graphite N (29.46%), respectively. The effective pyridine N and graphite N are expected to increase the ORR activity of the catalyst [40]. Additionally, the peaks at 288.5, 284.9 and 283.9 eV in the C1s high resolution spectrum (Fig. S2c in Supporting information) correspond to C-O, C-N/S, and C-C. The above results further confirm that nitrogen and sulfur have been successfully doped into carbon materials. As the synergistic effect of N and S co-doping, CoS_2/NSC-MC is expected to exhibit significant oxygen electrocatalytic activity [41].

The thermogravimetric analysis (Fig. S3 in Supporting information) was performed to examine the metal content of the composites. It can be seen that the loss weight of the sample below 200 °C is primarily due to the desorption of surface adsorbed water, the loss weight between 200 °C and 400 °C is primarily due to the oxidation of CoS_2, and the loss weight between 450 °C and 800 °C is primarily due to the simultaneous oxidation of carbonaceous matrix. Finally, the CoS_2 content can be calculated to be approximately 4.72%.

Scanning electron microscope (SEM) was used to examine the nano-micro structural morphology of the samples (Fig. S4 in Supporting information). The samples exhibit an irregular block morphology composed of bundle matrix, in which CP-SC exhibiting a relatively broken structure, whereas the other three composites exhibit a coherent structure, accompanied by CoS_2 nanocrystals on the surface of the composite. CoS_2/NSC-MC has a relative smooth surface and a better distribution of CoS_2 nanocrystals, which is attributable to the combined action of 2-methylimidazole and β-cyclodextrin in limiting and dispersing effect. Additionally, there are plenty filamentous crosslinking structures between the bundled matrix of CoS_2/NSC-MC (Fig. 2a). This structure might be the effect of catalysis on β-cyclodextrin decomposition by cobalt during the heat treatment. During the calcination process, the pitch melts and fills the pore of SBA-15 and then carbonizes. Simultaneously, because 2-methylimidazole also has an aromatic nucleus structure, it is compatible with pitch, enabling it to introduce coordination cobalt into the carbonaceous matrix during pitch carbonization. On the other hand, following dispersion of cobalt, β-cyclodextrins decompose at high temperatures and are catalysed by cobalt to generate micro-nano crosslinking between the bundles of composite. The fibre stripes are evident in the transmission electron microscope (TEM) graphic (Fig. 2b), confirming that the material is composed of carbon fibre bundles. CoS_2 nanocrystals with sizes ranging from ten to one hundred nanometers are embedded in the carbon matrix skeleton, and the composite structure of carbon layer and CoS_2 can be clearly observed (Figs. 2c and d). The patterns of selected area electron diffraction (SEAD) embedded in Fig. 2c could correspond to the crystal planes of CoS_2. Furthermore, the lattice stripes (Figs. 2e and f) of metal nanoparticles correspond to the cubic CoS_2 crystal planes (200) and (111), respectively, confirming the presence of CoS_2 nanocrystals in the materials. The distribution of C, Co, N, O, and S can be clearly seen in the TEM-EDS element mapping image of CoS_2/NSC-MC (Fig. 2g). The five elements are distributed relatively uniformly. Additionally, Fig. S5 (Supporting information) shows the atomic content derived using EDS, and the cobalt content (2.53%) is greater than that determined using XPS, verified that the CoS_2 is wrapped in the carbon layer.

Electrochemical tests were performed to discuss the ORR and OER performance. Cyclic voltammetrys (CVs) in a 0.1 mol/L KOH electrolyte saturated with N_2 or O_2 present oxygen reduction peak potential of materials (Fig. 3a). It can be seen that the potential of CoS_2/NSC-MC (0.835 V) is more positive compared with CoS_2/NSC-M (0.793 V), CoS_2/SC (0.781 V) and CP-SC (0.664 V), even higher than that of 20% Pt/C (0.826 V) (Fig. S6 in Supporting information), suggesting that CoS_2/NSC-MC has desirable ORR activity. The ORR polarisation curves of different samples were produced using linear sweep voltammetrys (LSVs) (Fig. 3b). It can be seen that the ORR performance of CP-SC is poor, while the half-wave potentials ($E_{1/2}$) of CoS_2/SC and CoS_2/NSC-M are 0.779 V and 0.791 V, respectively, indicating that the modified materials have strong catalytic ability, abundant N and S element doping and CoS_2 particles inside mesoporous carbon can greatly enhance the ORR activity of the compositesbut their largest diffusion-limiting current densities (J_i) are only 2.68 mA/cm^2 and 2.91 mA/cm^2, respectively, which is related to their irregular morphology and structure [42]. Notably, since the composition and structure of CoS_2/NSC-MC are suitable for ORR, it has the most positive $E_{1/2}$ (0.837 V) and the highest J_i (4.76 mA/cm^2), which is even superior to 20% Pt/C (0.830 V and 4.17 mA/cm^2). Moreover, the $E_{1/2}$ (0.812 V) and the J_i (4.37 mA/cm^2) of Co_3O_4/NC-MC (Fig. S7) is lower than CoS_2/NSC-MC. It is attributed to the unsaturated CoS_2 sites and S atom doping, which favors the chemisorption of OH- and oxygen-containing intermediates on the surface. Fig. 3c shows the Tafel slope of each sample, in which the CoS_2/NSC-MC (69.3 mV/dec) is best, even superior than that of 20% Pt/C (97.7 mV/dec). This result also agrees with the estimated kinetic current density (J_k) in Fig. 3d. At 0.83 V, the J_k of CoS_2/NSC-MC is 4.73 mA/cm^2, which is greater than the 4.17 mA/cm^2 of 20% Pt/C.

To further characterise the ORR catalytic route and kinetic behaviour of materials, the LSV tests under different rotational speeds were performed (Fig. S8 in Supporting information), and the corresponding K-L curves (Fig. S9 in Supporting information) were constructed according to K-L equation. Clearly, the linear relationship of CoS_2/NSC-MC indicates that the catalytic process of ORR follows first-order reaction kinetics, which is exclusively dependent on the concentration of O_2 in the electrolyte [43]. The results indicate that the number of ORR transmitted electrons (n) of CoS_2/NSC-MC (3.96) is the highest among the samples, approaching the theoretical value of 4 and even slightly surpassing that of 20% Pt/C (3.81) under the same conditions, but the n of ORR for pure carbon material (CP-SC) is only 2.05 (Fig. 3e). Samples containing CoS_2 have a higher n, indicating that these composites have improved ORR performance, and therein the CoS_2/NSC-MC presents the best ORR catalytic efficiency. By using rotating ring-disk electrode (RRDE) to measure the polarization curve of samples (Fig. S10 in Supporting information), and the n and hydrogen peroxide yield (Fig. 3f) were calculated.

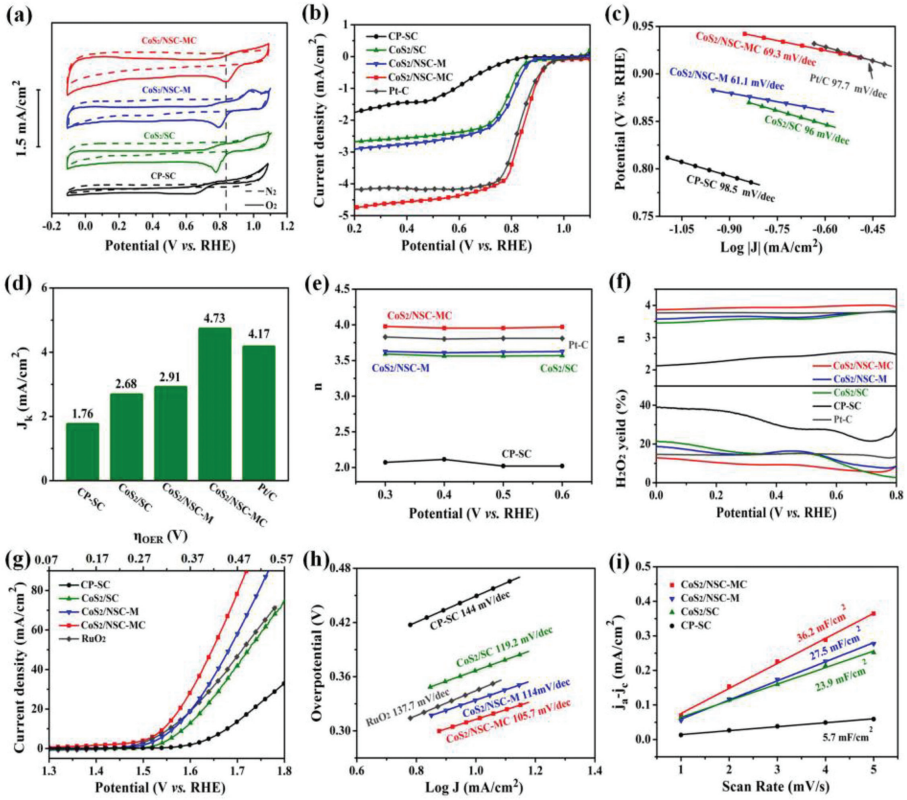

Fig. 3. (a) CVs of CP-SC, CoS_2/SC, CoS_2/NSC-M and CoS_2/NSC-MC. (b) LSVs, (c) Tafel plots, (d) J_k, (e) the number of electrons transferred (n) and (f) the peroxide yield and electron transfer number of CP-SC, CoS_2/SC, CoS_2/NSC-M, CoS_2/NSC-MC and Pt/C. (g) LSV curve, (h) corresponding Tafel slope and (i) linear fitting of the electrochemical active areas of CP-SC, CoS_2/SC, CoS_2/NSC-M, CoS_2/NSC-MC and RuO_2.

The results indicate that the CP-SC (n = 2.16) presents high yield of peroxide (38.7%), indicating that the ORR tends to be carried out by the $2e^-$ pathway. On the other hand, the n of ORR for CoS_2/SC (3.45), CoS_2/NSC-MC (3.56) and CoS_2/NSC-MC (3.87) is close to 4, and the corresponding hydrogen peroxide yields are 25.1%, 18.5% and 10.5%, respectively. The composites present superior ORR electrocatalytic efficiency, and CoS_2/NSC-MC is even slightly better than 20% Pt/C, which is due to its ideal structure.

Apart from high ORR electrocatalytic activity, cycle stability and resistance to methanol crossover are also required. The chronoamperometric response measurements (Fig. S11a in Supporting information) of 20% Pt/C and CoS_2/NSC-MC are performed before and after 3 mol/L methanol addition. The results clearly demonstrate that CoS_2/NSC-MC displayed greater tolerance to methanol than Pt/C. Fig. S11b (Supporting information) shows the ORR stability of CoS_2/NSC-MC and 20% Pt/C for 15000 s. In order to further elucidate the stability of CoS_2/NSC-MC in alkaline electrolyte, we carried out SEM and TEM characterizations of CoS_2/NSC-MC after testing the *i-t* curve for 15000 s. These carbon fiber bundles after testing becomes fragmented, as displayed in Fig. S12 (Supporting information). However, they still have a smooth block structure with clear fiber boundaries and the CoS_2 nanoparticles were further transformed into smaller particles, uniformly distributed in nitrogen-sulfur co-doped mesoporous carbons. It indicates that the CoS_2/NSC-MC catalyst has good stability in alkaline electrolyte.

Simultaneously, the OER electrocatalytic capabilities of the samples were also investigated. Dependent on the OER polarisation curve of the samples (Fig. 3g), the lowest OER overpotential (η_{OER}) of CP-SC upon the current density of 10 mA/cm^2 is 449 mV, indicating its slow OER ability, whereas other composite samples exhibit good OER performance, with the η_{OER} of CoS_2/NSC-MC (313 mV) being lower than that of the other two composites and even lower than that of RuO_2 (325 mV) and Co_3O_4/NC-MC (450 mV) (Fig. S13 in Supporting information). As expected, CoS_2 efficiently reduces the η_{OER} of material, and the micro-nano crosslinking structure of composite enhances the kinetic efficiency, revealing that CoS_2/NSC-MC exhibits the optimum electrocatalytic characteristics for OER. Additionally, the kinetic differences between the samples can be compared by using OER Tafel curves (Fig. 3h). According to the results, the Tafel slope of CoS_2/NSC-MC is 105.7 mV/dec, which is significantly less than that of RuO_2 (137.7 mV/dec). The OER stability is also important for the materials using in energy conversion device. The chronopotentiometry response measurements (Fig. S14 in Supporting information) of RuO_2 and CoS_2/NSC-MC are performed under potential of 1.5 V. After 30000 s, CoS_2/NSC-MC retains 95% of its original OER current density, whereas RuO_2 retains just 83%, demonstrating the high durability of CoS_2/NSC-MC. Electrochemically active surface area (ECSAs) can be estimated by testing CV at different scanning rates in the non-Faraday region (Fig. S15 in Supporting information) to determine double-layer capacitance (C_{dl}). The results shows that the C_{dl} of CP-S is only 5.7 mF/cm^2, while that of CoS_2/NSC is 23.9 mF/cm^2 (Fig. 3i), demonstrating that composite structure can significantly enhance ECSAs of materials. For CoS_2/NSC-MC, the C_{dl} is 36.2 mF/cm^2, which suggests that nitrogen doping and the dispersion of CoS_2 enhance the density of active sites. It reveals that the composite structure resulting in the large ECSAs of sample and finally increase the OER activity.

The reversible potential difference (ΔE), which is used to determine whether a material can be used as the bifunctional oxygen electrocatalyst, equals the difference between the lowest OER potential upon the current density of 10 mA/cm^2 ($E_j = 10$) and the ORR $E_{1/2}$. In general, the lower ΔE, the greater the bifunctional electrocatalytic activity of material. As shown in Fig. S16 (Support-

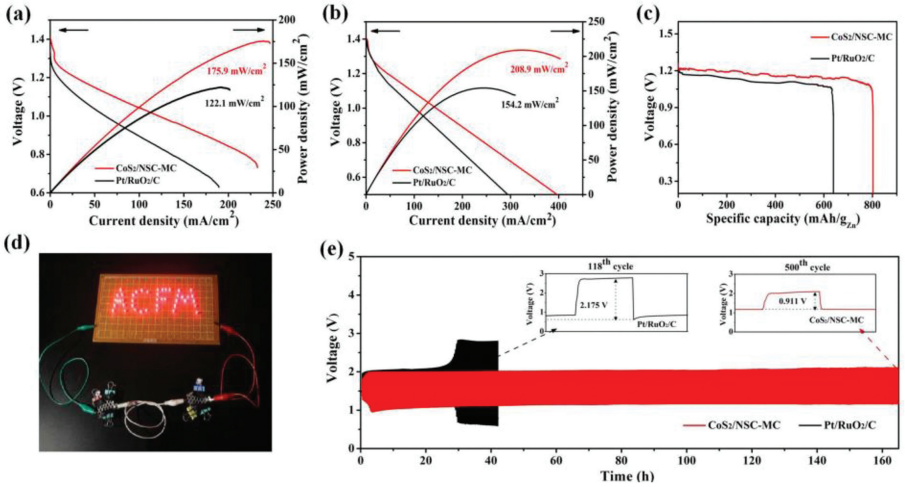

Fig. 4. (a) Discharge polarization and power density curves of CoS_2/NSC-MC and Pt/RuO_2/C all-solid-state zinc-air batteries. Comparison of performance for liquid Zn-air batteries driven by CoS_2/NSC-MC and Pt/RuO_2/C: (b) discharge polarization and power density curve, (c) discharge curve at 2 mA/cm^2, (d) Photograph of a lighted light emitting diode (LED) powered by the all-solid-state Zn-air batteries. (e) long-term cycling performance at a current density of 2 mA/cm^2 for liquid Zn-air batteries driven by CoS_2/NSC-MC and Pt/RuO_2/C.

ing information), the ΔE of CoS_2/NSC-MC is only 0.706 V, which is slightly less than that of Pt/RuO_2/C (0.726 V) and other samples, indicating that it is likely to be employed in reversible zinc-air batteries. The all-solid zinc-air battery was assembled with the

CoS_2/NSC-MC used as bifunctional catalyst (Fig. S17a in Supporting information). The power density results demonstrate that the maximum power density of CoS_2/NSC-MC is higher than that of Pt/RuO_2/C, which is 175.9 mW/cm^2 (Fig. 4a). Furthermore, the battery is discharged under the constant current of 2 mA/cm^2, and it is calculated that the specific capacity of CoS_2/NSC-MC can reach 1358.1 mAh/g_{Zn} (Fig. S18a in Supporting information), which is also higher than that of Pt/RuO_2/C. To further investigate the material stability in all-solid-state zinc-air battery, the charge-discharge cycle measurement (Fig. S18b in Supporting information) demonstrates that the CoS_2/NSC-MC are stable and can be cycled for more than 8 h, with a lower Coulomb efficiency decline than that of Pt/RuO_2/C. Two all-solid-state zinc-air batteries can be connected in series to power 43 LED light-emitting diodes continuously (Fig. 4d).

Additionally, a liquid zinc-air battery was also assembled (Fig. S17b in Supporting information). It can be found from Fig. 4b that the highest power density of zinc-air battery with CoS_2/NSC-MC (208.9 mW/cm^2) is much higher than that of zinc-air battery with Pt/RuO_2/C (154.2 mW/cm^2) as well as some recent reported catalysts (Table S2 in Supporting information). The constant current discharge test was conducted under the current density of 2 mA/cm^2 (Fig. 4c). The discharge voltage of the zinc-air battery with CoS_2/NSC-MC was found to be approximately 1.2 V, and its specific capacity was determined to be as high as 803.2 mAh/g_{Zn}. The charge-discharge cycle measurement (Fig. 4e) demonstrates that the zinc-air battery with CoS_2/NSC-MC shows excellent durability of more than 160 h and 500 cycles. Its charge-discharge potential difference is 0.911 V, which is superior to 2.175 V of Pt/RuO_2/C. The excellent performance is ascribed to the structure being optimised for oxygen electrocatalysis, the ordered pore and micro-nano crosslinking structure promotes charge transfer between CoS_2 and N,S co-doped mesoporous carbons, as well as oxygen species diffusion. In addition, the homogenous composite and doping structure improves catalytic active site activity. The results indicate that the synthesized CoS_2/NSC-MC composites as bifunctional oxygen electrocatalysts have a good prospect of increasing zinc-air battery charge and discharge performance, power density, specific capacity, and stability.

In conclusion, a straightforward strategy was used to develop a CoS_2 nanocrystal composite N/S doped ordered mesoporous carbon bifunctional OER/ORR electrocatalyst with an optimal structure. In this strategy, 2-methylimidazole and pitch are both aromatic to realize the compound of carbon and metal during heat treatment, β-cyclodextrin is used to disperse metal, and simultaneously form micro-nano crosslinking structure. The product exhibits superior ORR and OER activity and stability compare with noble metal catalysts. When utilised in reversible zinc-air battery, the composites perform admirably, achieving a maximum power density of 208.9 mW/cm^2 and excellent durability of more than 160 h and 500 cycles. This strategy paves the way for the production of stable, low-cost, high-performance metal-carbon composites, as well as for the research and development of viable energy conversion technologies.

Declaration of competing interest

The authors declare that they have no known competing financial interests or personal relationships that could have appeared to influence the work reported in this paper.

Acknowledgments

This research is supported by the National Natural Science Foundation of China (Nos. 52104301, 52171207, 52072120), the Scientific Research Fund of Hunan Provincial Education Department, China (Nos. 21A0392, 19A203, 21B0591), the Open-End Fund for Hubei Key Laboratory of Pollutant Analysis & Reuse Technology (Hubei Normal University) (No. PA190102), the Guangxi Key Laboratory of Low Carbon Energy Material (No. 2020GXKLLCEM03).

Supplementary materials

Supplementary material associated with this article can be found, in the online version, at doi:10.1016/j.cclet.2022.06.020.

References

[1] W. Jin, J. Chen, B. Liu, et al., Small 15 (2019) 1904210.
[2] F.L. Meng, K.H. Liu, Y. Zhang, et al., Small 14 (2018) 1703843.
[3] K. Huang, Y. Xu, Y. Song, et al., J. Mater. Sci. Technol. 65 (2021) 1–6.
[4] Y. Ren, H. Wang, T. Zhang, et al., Chin. Chem. Lett. 32 (2021) 2243–2248.
[5] S. Cheng, R. Zhang, W. Zhu, et al., Appl. Surf. Sci. 518 (2020) 146106.
[6] S. Tang, X. Wang, Y. Zhang, et al., Nanoscale 11 (2019) 2202–2210.

[7] W. Kong, X. Luan, H. Du, et al., Chem. Commun. 55 (2019) 2469–2472.
[8] S. Ju, Y. Liu, H. Chen, et al., ACS Appl. Energy Mater. 2 (2019) 4439–4449.
[9] S. Zhang, D. Zhai, T. Sun, et al., Appl. Catal. B 254 (2019) 186–193.
[10] D. He, X. Wu, W. Liu, et al., Chin. Chem. Lett. 30 (2019) 229–233.
[11] X. Gao, Z. Xu, G. Li, Chem. Eng. J. 431 (2022) 133385.
[12] L. Li, L. Song, H. Guo, et al., Nanoscale 11 (2019) 901–907.
[13] S.A. Patil, I. Rabani, D. Vikraman, et al., Int. J. Energy Res. 45 (2021) 2785–2796.
[14] X. Ma, W. Zhang, Y. Deng, et al., Nanoscale 10 (2018) 4816–4824.
[15] Z. Huang, Z. Yang, M.Z. Hussain, et al., Electrochim. Acta 330 (2020) 135335.
[16] J. Chen, J. Huang, H. Wang, et al., Chin. Chem. Lett. 33 (2022) 3752–3756.
[17] G. Zhang, X. Liu, P. Yu, et al., Chin. Chem. Lett. 33 (2022) 3903–3908.
[18] J. Han, H. Bao, J.Q. Wang, et al., Appl. Catal. B 280 (2021) 119411.
[19] Y. Xu, L. Zhu, X. Cui, et al., Nano Res. 13 (2020) 752–758.
[20] Y. Wu, J. Huang, Z. Lin, et al., Chem. Eng. J. 423 (2021) 130241.
[21] B. Wang, Y. Ye, L. Xu, et al., Adv. Funct. Mater. 30 (2020) 2005834.
[22] K. Wang, H. Chen, X. Zhang, et al., Appl. Catal. B 264 (2020) 118468.
[23] Z. Li, W. Wang, M.J. Zhou, et al., J. Energy Chem. 54 (2021) 310–317.
[24] X. Feng, Y. Bai, M. Liu, et al., Energy Environ. Sci. 14 (2021) 2036–2089.
[25] X. Wang, C. Yang, J. Li, et al., Adv. Funct. Mater. 31 (2021) 2009109.
[26] W. Xue, Q. Zhou, X. Cui, et al., Nano Energy 86 (2021) 106073.
[27] Y.Y. Chen, C.X. Xu, Z.H. Hou, et al., Mater. Today Energy 16 (2020) 100402.
[28] L. Chen, W.Q. Ren, C.X. Xu, et al., J. Alloys Compd. 894 (2021) 162038.
[29] X. Qin, Y. Huang, Y. Shen, et al., Ceram. Int. 45 (2019) 24515–24527.
[30] X.F. Lu, S.L. Zhang, E. Shangguan, et al., Adv. Sci. 7 (2020) 2001178.
[31] W. Li, Y. Li, H. Fu, et al., Chem. Eng. J. 381 (2020) 122683.
[32] W. Fang, Z. Bai, X. Yu, et al., Nanoscale 12 (2020) 11746–11758.
[33] W. Zhao, Y. Ye, W. Jiang, et al., J. Mater. Chem. A 8 (2020) 15822–15828.
[34] H. Wang, X. Qiu, Z. Peng, et al., J. Colloid Interface Sci. 561 (2020) 829–837.
[35] L. Guo, J. Deng, G. Wang, et al., Adv. Funct. Mater. 28 (2018) 1804540.
[36] P. Liu, S. Gao, X. Liu, et al., Compos. B Eng. 192 (2020) 107992.
[37] X. Li, T. Liu, Y.X. Wang, et al., J. Power Sources 451 (2020) 227790.
[38] H. Chen, M.Q. Wang, Y. Yu, et al., ACS Appl. Mater. Interfaces 9 (2017) 35040–35047.
[39] Z. Liu, Z. Zhao, Y. Wang, et al., Adv. Mater. 29 (2017) 1606207.
[40] Y. Xie, Y. Liu, Y. Yao, et al., Chin. Chem. Lett. 33 (2022) 1298–1302.
[41] Y. Tang, R. Liu, S. Liu, et al., Carbon 141 (2019) 704–711.
[42] H. Zhao, Y. Zhang, L. Li, et al., Chin. Chem. Lett. 32 (2021) 140–145.
[43] Y. Sun, J. Ouyang, J. Luo, et al., Chin. Chem. Lett. 32 (2021) 92–98.